Journal of Materials Chemistry A

PAPER

View Article Online
View Journal | View Issue

Cite this: J. Mater. Chem. A, 2017, 5, 14583

In situ grown cobalt selenide/graphene nanocomposite counter electrodes for enhanced dye-sensitized solar cell performance†

Vignesh Murugadoss,[a] Ning Wang,*[b] Sruthi Tadakamalla,[c] Bin Wang,[b] Zhanhu Guo *[c] and Subramania Angaiah *[a]

Received 29th January 2017
Accepted 7th June 2017

DOI: 10.1039/c7ta00941k

rsc.li/materials-a

Graphene nanocomposites were prepared by *in situ* hydrothermally growing CoSe nanoparticles on different amounts of graphene nanosheets (GNs). The influence of graphene content on the physical and electrochemical properties of CoSe was studied. The CoSe nanoparticles with high catalytic activity accelerated the reduction of triiodide, while the graphene facilitated charge transport during the catalytic process. The CoSe/$GN_{0.50}$ displayed the highest catalytic activity due to its lowest charge transfer resistance. With increasing the graphene content beyond the optimum concentration, restacking of graphene caused a decreased electrocatalytic activity of CoSe/GN nanohybrids. The DSSCs fabricated with CoSe/$GN_{0.50}$ as the CE exhibited 20% improvement in the photo-conversion efficiency (PCE) with respect to the standard Pt, much higher than using other reported binary metal selenides. This revealed that CoSe/$GN_{0.50}$ nanohybrids could be used as a promising alternative to platinum counter electrodes for DSSCs.

1. Introduction

Since the first demonstration in 1991, dye-sensitized solar cells (DSSCs) have attracted great interest because of their merits such as low cost, easy fabrication and relatively high power conversion efficiency (PCE).[1] At present, DSSCs offer a credible alternative to the traditional solid state devices, a technically and economically promising solution to energy depletion, environmental pollution and ecological destruction. DSSCs have been proved to perform better than conventional solar cells, without a significant change in the PCE in diffused light.[2] As a key component, the role of the counter electrode (CE) is to collect electrons from the external circuit and catalyze the reduction of triiodide (I_3^-) to iodide (I^-) at the CE/electrolyte interface.[3,4] Hence, an efficient CE should have excellent electrocatalytic activity, high electrical conductivity, a large specific surface area, and high corrosion stability against iodine in the electrolyte. Usually, platinum (Pt) is used to catalyze the reduction of I_3^- due to its superior conductivity and electrocatalytic activity. However, the factors, such as low abundance ratio, high cost and formation of PtI_4 or H_2PtI_6 due to the corrosion by the I^-/I_3^- redox couple, prevent noble metal Pt from being used for large-scale manufacturing of DSSCs. This has stimulated great efforts to exploit substitutes for Pt in order to reduce the overall cost and simultaneously keep the performance of DSSCs.[5] Various carbon materials, conducting polymers, sulfides, nitrides, carbides and their composites/hybrids have been reported as CE materials in place of Pt.[6,7]

Semiconducting metal selenides have drawn enormous attention due to their unique electronic properties, attractive chemical behaviors and wide range of potential applications.[8–11] For example, Wang *et al.* reported the utilization of metal selenides ($Co_{0.85}Se$ and $Ni_{0.85}Se$) as CEs in DSSCs. These metal selenides exhibited much higher electrocatalytic activity than Pt towards I_3^- reduction, and generated a promising efficiency of 9.40% for DSSCs.[8c] Jia *et al.* achieved a cell efficiency of 8.88% by using nickel selenide ($Ni_{0.85}Se$) as the CE which is higher than that of Pt CEs (8.13%).[9] Duan *et al.* reported 10% cell efficiency using $Ni_{0.85}Se$ as the CE.[10] Lee *et al.* reported a PCE of 8.31% for the cells with urchin-like Ni_3Se_4@MeOH CE which is higher than that of the Pt CE (8.03%) for DSSCs.[11] However, there will be a slowdown of electrons flowing from the external circuit to the metal selenide/electrolyte interface due to the relatively poor connection between them, thus retarding the tri-iodide (I_3^-) reduction. Also, the aggregation of nanoparticles resulted in a decreased active surface area which reduced the electrocatalytic activity. To overcome these drawbacks, hybridization of these materials with conductive carbon based materials such as activated carbon, carbon nanotubes (CNTs), graphene, *etc.* is

[a]Electrochemical Energy Research Lab, Centre for Nanoscience and Technology, Pondicherry University, Puducherry-605 014, India. E-mail: a.subramania@gmail.com
[b]Engineered Multifunctional Composites (EMC) Nanotech. LLC, Knoxville, TN 37934, USA. E-mail: wangninguestc@gmail.com
[c]Integrated Composites Laboratory (ICL), Department of Chemical and Biomolecular Engineering, University of Tennessee, 322, Dougherty Engineering Bldg., Knoxville, TN 37996, USA. E-mail: zguo10@utk.edu; nanomaterilas2000@gmail.com

† Electronic supplementary information (ESI) available. See DOI: 10.1039/c7ta00941k

in the limelight and has shown promise to boost the conductivity and catalytic activity of the materials at the same time.[12–14]

Metal sulfide loaded graphene has been reported as the CE for DSSCs and its PCE is comparable to that of standard platinum.[15–17] Moreover, the more electronegativity of sulfur may render the metal sulfide structure more ionic than metal selenides and hence a larger electrical resistivity is expected for sulfides than selenides.[18] Therefore, it is desirable to synthesize CoSe/GN nanohybrids to serve as an efficient CE for DSSCs. Among various processes to prepare CoSe such as hot injection,[19] microwave irradiation,[20] high temperature dissolution–reprecipitation,[21] and thermal decomposition,[22] the hydrothermal process is a facile route for large scale synthesis. Also, the physical and electrochemical properties of the CoSe/GN nanohybrids can be tuned by varying the mass ratio of graphene and cobalt selenide. However, there is no report on metal selenide loaded graphene as the CE for DSSCs yet.

Herein, for the first time, cobalt selenide nanoparticles with different loadings were *in situ* grown on graphene by a simple hydrothermal method. The structure, morphology and composition were confirmed by X-ray diffraction (XRD), Raman spectroscopy, field emission scanning electron microscopy (FE-SEM), transmission electron microscopy (TEM) and X-ray photoelectron spectroscopy (XPS). The feasibility of these hybrid nanocomposites to serve as CEs for DSSCs was tested. The influences of the graphene content on the electrical conductivity, catalytic activity, and electrochemical and photovoltaic performances were studied. The electrochemical activities of these prepared CoSe and CoSe/GN nanohybrids were investigated using electrochemical impedance spectroscopy (EIS), cyclic voltammetry (CV) and Tafel polarization studies. The CoSe/$GN_{0.50}$ nanocomposites showed excellent electrocatalytic behaviour and thus led to a higher PCE. The DSSC was then fabricated with a CoSe/$GN_{0.50}$ based CE and its photovoltaic performance was compared with those fabricated with standard Pt based CEs and other reported binary metal selenide based CEs.

2. Experimental

2.1 Materials

Cobalt chloride hexahydrate ($CoCl_2 \cdot 6H_2O$, 98% pure), sodium nitrate ($NaNO_3$, 99% pure), iodine (I_2, 98% pure), hydrazine hydrate ($N_2H_4 \cdot H_2O$, 99–100% pure), *N*-methyl-2-pyrrolidone (NMP, 99% pure) and sulfuric acid (H_2SO_4, 98% pure) were purchased from Merck. Graphite flakes (99.5%) and lithium perchlorate ($LiClO_4$, 99% pure) were purchased from HIMEDIA. Potassium permanganate ($KMnO_4$, 99.5% pure) and lithium iodide (LiI, 98% pure) were procured from Sisco Research Laboratories Pvt. Ltd. The selenium powder (Se, >99.5% trace metal basis), polyvinylidene fluoride (PVDF, molecular weight = 530 000), 4-*tert*-butylpyridine (TBP, 96% pure), 1-butyl-3-methylimidazolium iodide (BMImI, 99% pure) and acetonitrile (99.5% pure) were obtained from Sigma-Aldrich. The ITO coated glass slides were obtained from Sigma Aldrich (surface conductivity ~ 8–12 Ω sq^{-1}). The TiO_2 and platinum paste were purchased from Dyesol Ltd. and the dye Di-tetrabutylammonium *cis*-bis(isothiocyanato)bis(2,2′-bipyridyl-4,4′-dicarboxylato) ruthenium(II) was procured from Sigma-Aldrich. All the chemical reagents were of analytical grade and used as received.

2.2 Preparation of CoSe/GN nanohybrids

The CoSe/GN nanohybrids were prepared by a simple hydrothermal method. Briefly, 0.0345 g cobalt chloride hexahydrate ($CoCl_2 \cdot 6H_2O$) and 0.01145 g selenium (Se) powders were taken in a 1 : 1 mole ratio and then dissolved in 50 mL deionized water. To this, the required quantity of graphene oxide (0.02 g) prepared by a modified Hummers method[23,24] was dispersed under ultrasonication to obtain CoSe/GN nanohybrids with a CoSe to graphene mass ratio of 1 : 1. Hydrazine (10 mL) was then added drop by drop with constant stirring to act as a reducing agent to increase the graphitization nature of graphene as well as for the reduction of Co^{2+} to form cobalt selenide nanoparticles on the graphene. This mixture was transferred into a Teflon-lined stainless steel autoclave and kept at 120 °C for 12 h. After being cooled down to room temperature, the obtained precipitate was washed several times with distilled water and kept inside a vacuum oven at 50 °C for 12 h to obtain the CoSe/GN nanohybrids. By adopting this preparative procedure, the CoSe/GN nanohybrids with other mass ratios of CoSe and graphene such as 1 : 0.25, 1 : 0.50 and 1 : 0.75 were prepared and represented as CoSe/$GN_{0.25}$, CoSe/$GN_{0.50}$ and CoSe/$GN_{0.75}$, respectively. Pure CoSe nanoparticles were also prepared under the same reaction conditions without adding graphene oxide for comparison.

2.3 Fabrication of counter electrodes

The ITO glass slides were washed with acetone, ethanol and deionized water in an ultrasonic water bath and then dried in air. The ITO glass plate was chosen due to its low surface roughness and higher transmittance compared with FTO glass plates.[25] The film thickness was controlled using scotch tape as a spacer. The CEs of CoSe and CoSe/GN nanohybrids were prepared by slurry coating procedures. Approximately 95 wt% of the prepared CE material along with 5 wt% polyvinylidene fluoride (binder) were dispersed in the required amount of *N*-methyl-2-pyrrolidone (NMP) and then ground finely using a mortar to get the corresponding CE slurry paste. The as-prepared slurry was coated on the pretreated ITO substrate by using the doctor blade technique at a thickness of 15 μm and then dried for 12 h at 80 °C in a vacuum oven.[26] The images of the counter electrode materials are shown in Fig. S1.†

The reference Pt electrode was prepared by spreading platinum paste (Dyesol Ltd.) in the space between the scotch tape and the conducting glass substrate by using a doctor blade technique, followed by drying and sintering in air at 450 °C for 30 min at a heating rate of 5 °C min^{-1}.[27]

2.4 Physical characterization

The morphologies and nanostructures of the prepared CoSe nanoparticles and CoSe/GN nanohybrids were assessed by

using field emission scanning electron microscopy (JSM, JEOL 7600F) and high-resolution transmission electron microscopy (Philips, Model: CM 200). X-ray photoelectron spectroscopic (XPS) data were acquired using a Kratos AXIS Ultra DLD (Kratos Analytical Ltd.), with an X-ray source of mono Al Kα (1486.71 eV, 5 mA) and an operation power of 75 W. Unless mentioned otherwise, the data were acquired at an angle of 90° between the substrate and detector, with a step size of 1 eV and dwell time of 100 ms. Fitting and deconvolution of peaks were carried out using XPSPEAK 4.1 software. The peaks were referenced with respect to the C 1s peak at 284.6 eV.

The information about the phase and crystallinity was obtained by using the X-ray diffraction technique (Rigaku, Ultima IV) with nickel-filtered Cu-Kα radiation in the range of 20 to 80° with an increment of 0.02°. The Raman spectra were recorded by using a confocal micro-Raman spectrometer (Renishaw RM 2000) under a 20 mW Innova Ar ion laser of 514 nm.

2.5 Electrochemical characterization

Electrochemical impedance (EIS), cyclic voltammetry (CV), and Tafel polarization measurements were performed to evaluate the electrochemical catalytic activity of the nanocomposites prior to the fabrication of DSSC devices. The electrochemical impedance measurements were carried out by using a symmetric cell to test the electrocatalytic activities of the fabricated CEs. The frequency limit was set between 1 mHz and 100 kHz with an AC amplitude of 10 mV.[28]

Cyclic voltammetry measurements were performed in a three electrode cell consisting of platinum as the counter electrode, Ag/AgCl as the reference electrode, and one of the fabricated CEs as the working electrode in acetonitrile containing 0.01 M LiI, 0.001 M I_2 and 0.1 M $LiClO_4$ at the scan rate of 50 mV s^{-1}.[13]

Tafel polarization measurements were used to further test the electrocatalytic activity and analyze the interfacial charge transfer between the electrodes and electrolyte by using an electrochemical workstation (Biologic: VSP) at a scan rate of 50 mV s^{-1}. The Tafel polarization curves show the current density (J) as the function of voltage (V) for the symmetric cells fabricated by using the prepared CEs. The symmetrical dummy cells were assembled with two identical CEs coated on an ITO glass substrate with the redox electrolyte to be used for DSSCs.[29]

2.6 Fabrication of dye-sensitized solar cells (DSSCs)

The DSSCs were prepared following the published procedures.[30–32] Briefly, a thin layer of nonporous TiO_2 film was deposited on cleaned FTO, using 5% titanium(IV) butoxide in ethanol by spin-coating followed by annealing at 450 °C for 30 min. Then, the TiO_2 paste (Dyesol Ltd) was coated on the conducting glass substrate using the doctor blade technique and it was sintered at 450 °C for 30 min. After cooling down to room temperature, the TiO_2 electrodes were immersed into a 0.12 M $TiCl_4$ solution at 70 °C for 30 min. After rinsing with water, the electrodes were sintered at 450 °C for 30 min. The sintered photoanodes were dipped in a solution containing 3×10^{-4} M dye, Di-tetrabutylammoniumcis-bis(isothiocyanato) bis(2,2′-bipyridyl-4,4′-dicarboxylato) ruthenium(II) (Sigma-Aldrich) for 24 h. After the adsorption of the dye, the films were rinsed with pure ethanol to remove excess dye and then dried in hot air. The DSSCs were assembled using a TiO_2 photoanode with various CEs such as standard Pt (Dyesol Ltd.), CoSe and $CoSe/GN_{0.50}$ individually by a hot press at 110 °C. The I^-/I_3^- redox electrolyte containing 0.5 M LiI, 0.05 M I_2, 0.5 M TBP and 0.5 M 1-butyl-3-methylimidazolium iodide (ionic liquid) in acetonitrile was injected into the DSSCs *via* two small holes drilled on the CE side. Finally, the holes were sealed with the aid of small squares of Surlyn strips. The resultant active area of the cells was found to be 0.20 cm^2. All the fabrication steps and characterization measurements were carried out in an ambient environment without a protective atmosphere.

2.7 Photovoltaic performance of DSSCs

The photovoltaic performance of DSSCs was measured by using a calibrated AM 1.5 solar simulator (Newport, Oriel instruments U.S.A 150 W, Model: 67005) with a light intensity of 100 mW cm^{-2} and a computer controlled digital source meter (Keithley, Model: 2420). The *I–V* measurements were carried out on the DSSCs after an aging period of 24 h. The photoelectrochemical parameters, *i.e.*, the fill factor (FF) and light-to-electricity conversion efficiency (η) were calculated with eqn (1) and (2), respectively.[33]

$$\eta\ (\%) = \frac{V_{max}J_{max}}{P_{in}} \times 100 = \frac{V_{oc}J_{sc}FF}{P_{in}} \times 100 \quad (1)$$

$$FF = \frac{V_{max}J_{max}}{V_{oc}J_{sc}} \quad (2)$$

where J_{sc} is the short-circuit current density (mA cm^{-2}), V_{oc} is the open-circuit voltage (V), P_{in} is the incident light power (mW cm^{-2}), and J_{max} and V_{max} are the current density (mA cm^{-2}) and voltage (V) in the *J–V* curves, respectively, at the point of maximum power output. All the fabrication steps and characterization measurements were carried out in an ambient environment without a protective atmosphere. The values for the DSSCs were averaged over at least five measurements and were carried out under the same conditions. The detailed photovoltaic parameters calculated for the three systems of five DSSC devices made using identical counter electrode materials are summarized in Tables S1–S3.†

3. Results and discussion

Fig. 1a–e show the FE-SEM images of CoSe nanoparticles, graphene oxide (GO) and CoSe/GN nanohybrids. Pure CoSe nanoparticles are observed to aggregate to form large clusters, Fig. 1a. Fig. 1b shows that pure graphene oxide possesses a two-dimensional thin wrinkle sheet-like structure. At the mass ratio of 1 : 0.25 of CoSe to graphene, the graphene and agglomerated CoSe are almost disassociated and there is no connection between them, Fig. 1c. Fig. 1d depicts the CoSe/GN nanohybrids with a mass ratio of 1 : 50. The graphene prevents the aggregation of CoSe nanoparticles and forms porous conductive network structures. The functional groups in the graphene oxide could serve as active sites for the nucleation of CoSe

nanoparticles and these interactions led to a homogenous distribution of CoSe nanoparticles onto the graphene. The graphene with a large surface area provides an enhanced surface to volume ratio for increasing the contact area. Further, with increasing the mass ratio of CoSe to graphene beyond 1 : 0.50, the graphene gets restacked due to the π–π interactions and van der Waals forces between the planar basal planes of graphene nanosheets, for CoSe/$GN_{0.75}$ and CoSe/$GN_{1.00}$, respectively, Fig. 1e and f. Most of the CoSe nanoparticles are observed to be wrapped by graphene and only very few are dispersed on the graphene surface.

Fig. 2 depicts the HRTEM microstructures of the CoSe nanoparticles and CoSe/$GN_{0.50}$ nanohybrids. From the HRTEM image of CoSe nanoparticles, Fig. 2a, the sphere-shaped CoSe nanoparticles are observed with an average mean diameter of 14 nm. The CoSe nanoparticles are observed to be homogeneously distributed on the graphene nanosheets for the CoSe/$GN_{0.50}$ nanohybrid, Fig. 2b. This may be due to the oxygen containing functional groups such as –OH and –COOH on graphene nanosheets which act as the preferential sites for Co^{2+} adsorption. The Co^{2+} ions get adsorbed by these oxygen containing functional groups that exist abundantly on the edge and basal plane of graphene nanosheets. Thus, during the hydrothermal reaction, the CoSe nanoparticles will grow on the surface of graphene oxide without any agglomeration. The wrinkles found in the graphene sheets provide sufficient contact between the graphene and CoSe nanoparticles that bestows an enhanced conductivity to the CoSe/$GN_{0.50}$ nanohybrid. Fig. 2c depicts the clear lattice fringes which confirm good crystallinity of the CoSe/$GN_{0.50}$ nanohybrid.[34] Fig. 2c shows the lattice fringe spacings of 2.69, 2.02 and 1.80 Å, corresponding to the (101), (102) and (110) planes of hexagonal CoSe, respectively and the interlayer spacing of 3.45 Å ascribed to the graphene sheets of 3 to 9 graphitic layers, Fig. 2c.[12] In the selected area electron diffraction (SAED) pattern of the CoSe/$GN_{0.50}$ nanohybrids, Fig. 2d, the rings are indexed as (101), (102) and (110) of the hexagonal CoSe, indicating that the CoSe nanoparticles on the graphene sheets are polycrystalline in nature.

XPS was employed to explore the nature of chemical bonding and chemical state of CoSe/GN nanohybrids. The survey spectrum of CoSe/$GN_{0.50}$ nanohybrids, Fig. 3a, clearly shows the peaks of C 1s, O 1s, Co 2p, and Se 3d originating from graphene and CoSe in the nanohybrids.[35] The presence of the O 1s peak was due to the unavoidable surface oxygen adsorption of the hybrids from the environment.[36] The carbon peak at 284.6 eV, Fig. 3b, corresponds to the C–C peak, whereas the peak at 284 eV corresponds to the sp^2 hybridized carbon atoms (C=C) from the graphene. The C=C bond of the sp^2 structure contributes to the high electrical conductivity of graphene nanosheets. The Co 2p peaks, Fig. 3c, at 780.1 and 791.07 eV correspond to Co $2p_{3/2}$ and Co $2p_{1/2}$ representing the characteristics of Co^{2+}. The Se 3d peaks, Fig. 3d, at 54.9 and 58.8 eV are ascribed to Se $3d_{5/2}$ and Se $3d_{3/2}$, referring to the metal–selenide bond (Co–Se bonds of cobalt selenide).[37] From the XPS observations, it is revealed that the CoSe/GN nanohybrids mainly contain C, Co^{2+}, and Se^{2-}, indicating the formation of CoSe nanoparticles on the graphene nanosheets.

Fig. 4a shows the Raman spectra of pristine CoSe nanoparticles and CoSe/GN nanohybrids. Graphene oxide (GO) exhibits the D line at 1340 cm^{-1} and G line at 1582 cm^{-1}. The I_D/I_G ratio for GO was found to be 0.71. The Raman modes of CoSe

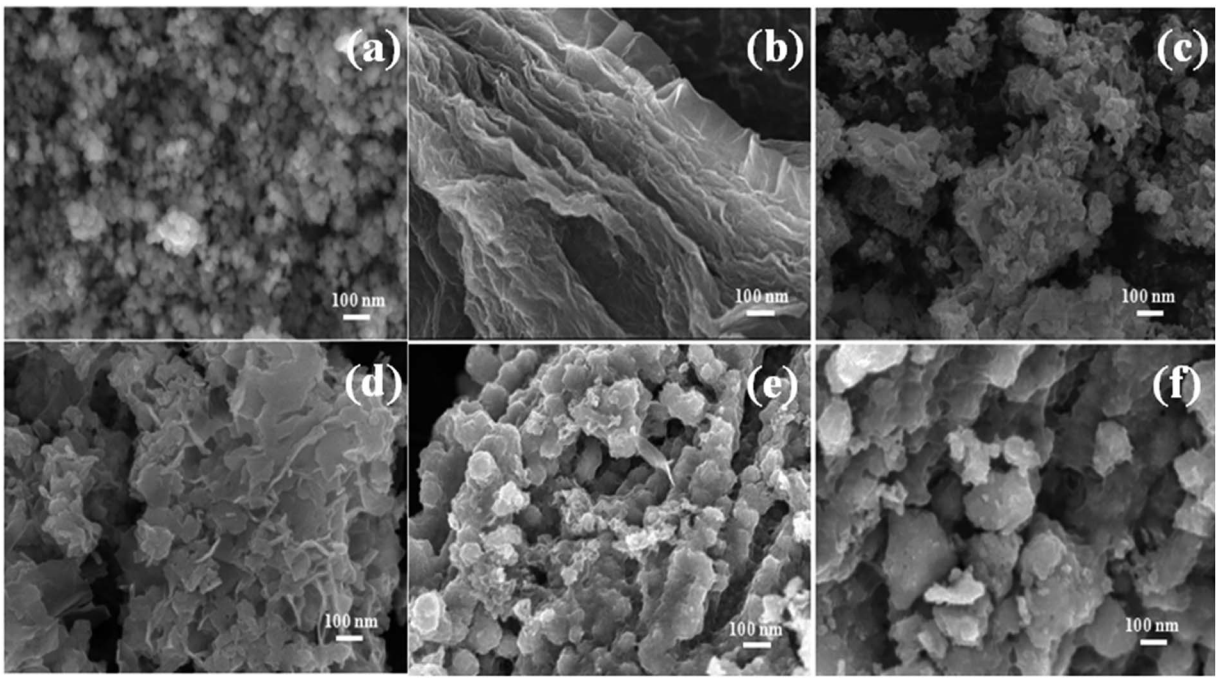

Fig. 1 FE-SEM images of (a) CoSe nanoparticles, (b) graphene oxide, (c) CoSe/$GN_{0.25}$, (d) CoSe/$GN_{0.50}$, (e) CoSe/$GN_{0.75}$ and (f) CoSe/$GN_{1.00}$ nanohybrids.

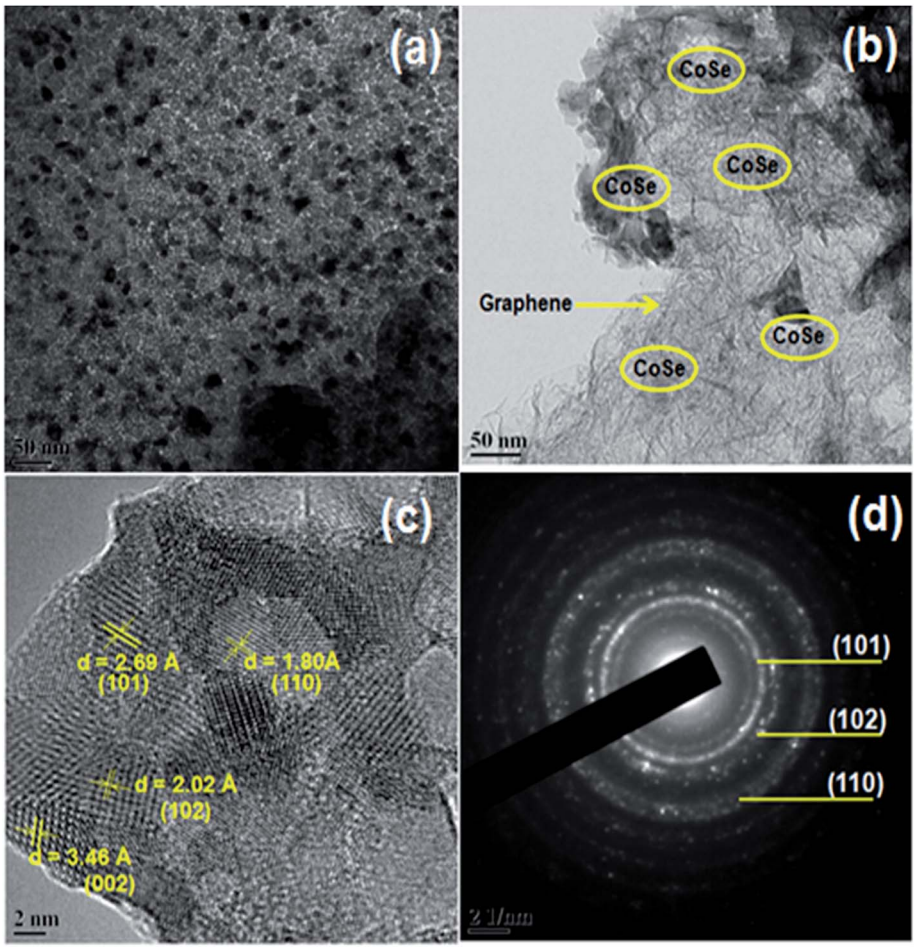

Fig. 2 TEM image of (a) CoSe nanoparticles, (b) CoSe/$GN_{0.50}$ nanohybrids, and (c) CoSe/$GN_{0.50}$ nanohybrids; (d) SAED of the image of CoSe/$GN_{0.50}$ nanohybrids.

were observed at around 160, 477 and 690.74 cm^{-1}.[38,39] In the Raman spectra of CoSe/GN nanohybrids, the D band at around 1340 cm^{-1} and G band at around 1582 cm^{-1} are observed, the characteristic peaks of graphene. The I_D/I_G ratio for CoSe/$GN_{0.25}$, CoSe/$GN_{0.50}$, CoSe/$GN_{0.75}$ and CoSe/$GN_{1.00}$ is 1.36, 1.40, 1.27 and 1.26, respectively. The higher I_D/I_G ratio of CoSe/GN nanohybrids than that of graphene oxide is due to the removal of oxygen functional groups in the graphene oxide sheets and the re-establishment of numerous small conjugated G-networks (sp^2 domains) during the reduction process.[40] The increase in the I_D/I_G ratio with increasing the graphene content can be ascribed to an increase in the degree of defects due to the shrinkage in the volume occupied by the graphene sheets upon the removal of oxygen.[41] The increased defect density caused more elastic scattering and thus contributed to the increasing I_D/I_G ratio. After the mass ratio of 1 : 0.50, more amorphous carbon resulting from the increased defect density attenuates all Raman peaks and thus the I_D/I_G ratio gets decreased.[42] It is observed that there is no change in the vibrational mode of CoSe in the CoSe/GN nanohybrids. This indicates no phase change in the CoSe nanoparticles with the addition of graphene.

Fig. 4b shows the XRD patterns of CoSe and CoSe/GN nanohybrids. The XRD patterns of CoSe are in good agreement with the reported literature.[43] The diffraction peaks at around 33.62°, 45.43°, 50.45°, 60.39 ° and 61.87° correspond to the (101), (102), (110), (103) and (112) planes of hexagonal CoSe, respectively.[44] The diffraction peaks match well with the diffraction rings of the SAED patterns. The intensity of the diffraction peak for graphene at around 25° is lower for CoSe/$GN_{0.25}$ and CoSe/$GN_{0.50}$ than that of CoSe/$GN_{0.75}$ and CoSe/$GN_{1.00}$ due to the prevention of aggregation and restacking of graphene by the immobilized CoSe nanoparticles.[13] The broad peak appearing at about 2θ = 19–40° is due to the disordered graphene in the nanohybrids.[16] The widening of diffraction peaks for CoSe in CoSe/GN nanohybrids implies that the size of CoSe is decreased in nanohybrids compared to pure CoSe nanoparticles. The mean particle size calculated from the peak at 2θ = 33.62, by using Scherrer's equation, is 17.25, 17.68, 13.41, 13.45 and 13.52 nm for CoSe, CoSe/$GN_{0.25}$, CoSe/$GN_{0.50}$, CoSe/$GN_{0.75}$ and CoSe/$GN_{1.00}$, respectively. Beyond the mass ratio of 1 : 0.50, the decrease in the intensity of CoSe peaks is due to the restacking of graphene that wraps the CoSe nanoparticles. The CoSe/$GN_{0.50}$ with smaller CoSe nanoparticles (~13.41 nm) offers a high accessible surface for the electrolyte.

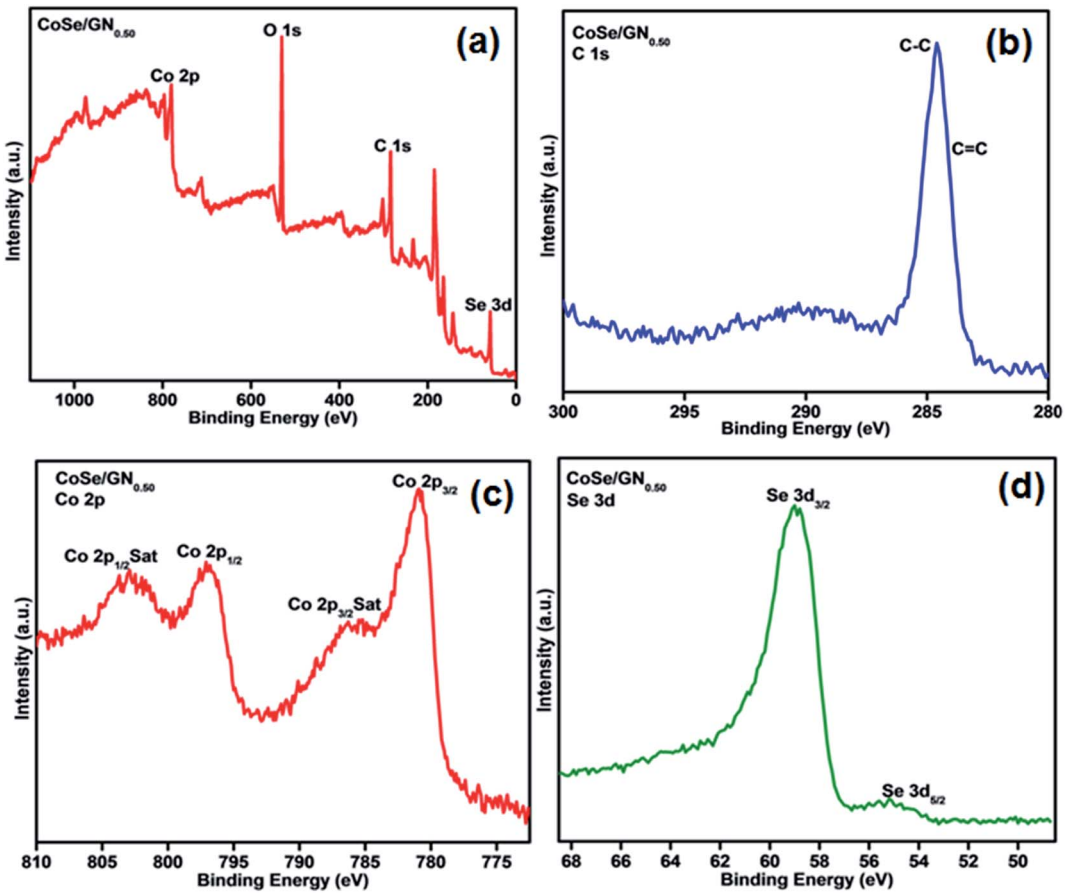

Fig. 3 (a) The survey XPS spectra; (b) C 1s XPS spectra; (c) Co 2p XPS spectra, and (d) Se 3d XPS spectra of the CoSe/$GN_{0.50}$ nanohybrids.

No impurity peaks are observed, confirming that the hydrothermal method is a facile approach to obtain pure hexagonal cobalt selenide. Fig. S2† shows the energy dispersive X-ray analysis (EDX) of CoSe nanoparticles and CoSe/$GN_{0.50}$ nanohybrids, respectively. The EDX revealed that the C, Co and Se species are present in the CoSe/GN nanohybrids. The atomic percentages of Co and Se are found to be 47.62 and 52.38, respectively, and hence the corresponding stoichiometric ratio of CoSe is confirmed as $Co_{0.90}Se$.

Fig. 5 shows the Nyquist plots of symmetrical cells fabricated with platinum, CoSe and CoSe/GN nanohybrids. The inset shows the equivalent circuit where R_s is the series resistance representing the resistance of the substrate in the higher frequency region, R_{ct} is the charge transfer resistance at the

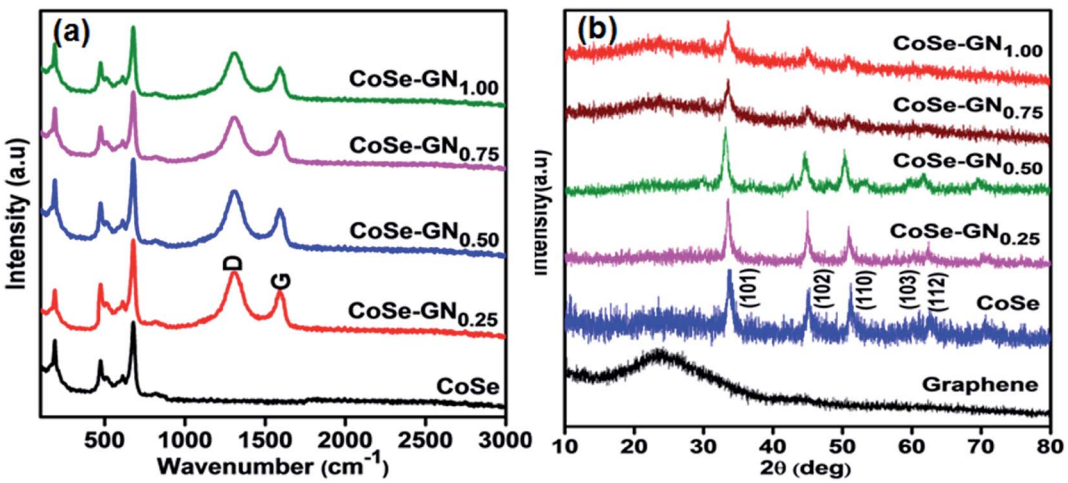

Fig. 4 (a) Raman spectra and (b) XRD patterns of CoSe nanoparticles and CoSe/GN nanohybrids.

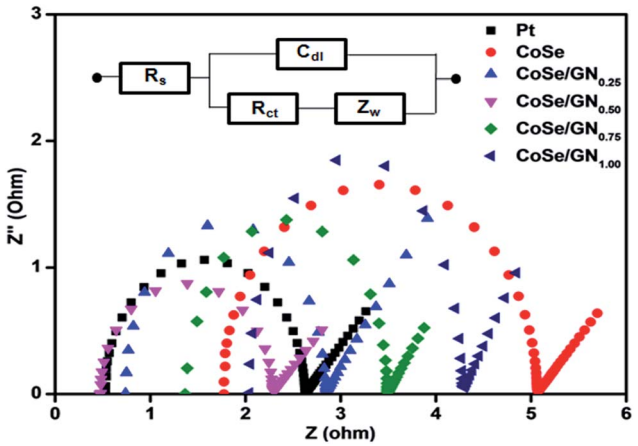

Fig. 5 Nyquist plots of symmetrical cells fabricated with platinum, CoSe and CoSe/GN nanohybrid CEs.

Table 1 Nyquist, cyclic voltammetry and Tafel polarization parameters of platinum, CoSe and CoSe/GN nanohybrids

Counter electrode	R_s (Ω cm^{-2})	R_{ct} (Ω cm^{-2})	D_n (cm^2 s^{-1})	J_0 (mA cm^{-2})
Pt	0.52	2.06	1.49×10^{-6}	6.23
CoSe	1.77	3.25	2.56×10^{-6}	3.95
CoSe-GN$_{0.25}$	0.74	2.12	2.87×10^{-6}	6.06
CoSe-GN$_{0.50}$	0.47	1.83	4.19×10^{-6}	7.02
CoSe-GN$_{0.75}$	1.36	2.13	2.79×10^{-6}	6.03
CoSe-GN$_{1.00}$	1.97	2.16	1.22×10^{-6}	5.94

electrode–electrolyte interface, and C_{dl} is its corresponding capacitance, and Z_w is the Nernst diffusion impedance in the lower frequency region.[45] The equivalent circuit is used to analyze the impedance spectra fitted by using EC lab software. The measured values of R_s and R_{ct} are given in Table 1. The CoSe/GN$_{0.50}$ CE shows superior electrocatalytic activity for I_3^- reduction compared to other CEs, including the platinum one. The addition of highly electrically conductive graphene nanosheets into CoSe nanoparticles enhances the shuttling of electrons from the external circuit to the high electrocatalytic CoSe, thereby increasing the reaction kinetics of triiodide reduction. However, the addition of graphene nanosheets beyond 50% increases the R_s and R_{ct} due to the aggregation of graphene nanosheets that blocks the diffusion of the electrolyte into the active sites of CoSe nanoparticles in the nanohybrids. The lower R_s value indicates that the CoSe/GN$_{0.50}$ has a good conducting performance arising from efficient electron transfer from the external circuit to the CoSe by the two-dimensional conductive network of graphene. Relatively lower R_{ct} values for CoSe/GN$_{0.50}$ indicate a faster charge transfer rate than those of other CoSe/GN nanohybrids. This results in a reduced interface loss of charge transportation and also enhances the charge collection efficiency, thereby increasing the photocurrent and fill factor of DSSCs.[13]

Fig. 6a shows the cyclic voltammogram (CV) curves of the CoSe and CoSe/GN nanohybrids. Two typical pairs of redox peaks (Oxd$_1$/Red$_1$ and Oxd$_2$/Red$_2$) of the CEs in the electrolyte containing I_3^-/I^- redox couples are clearly observed, corresponding to the reactions $3I_2^- + 2e^- \leftrightharpoons 2I_3^-$ and $I_3^- + 2e^- \leftrightharpoons 3I^-$. The cathodic peak current density (J_{pc}) in the second redox couple (Oxd$_2$/Red$_2$) and the separation (E_{pp}) between Oxd$_2$ and Red$_2$ peaks are the measures of the catalytic activity of CEs.[46] The cathodic peak of the CoSe nanoparticles appears at a comparatively more negative potential than that of the CoSe/GN nanohybrids. The enhanced electrocatalytic activity of the CoSe/GN nanohybrids can be attributed to the synergistic effect of superior electrical conductivity of graphene nanosheets and the superior electrocatalytic activity of CoSe nanoparticles.[8] The values of cathodic current (J_{pc}) show the trend of CoSe/GN$_{0.50}$ (−0.87 mA cm^{-2}) > CoSe/GN$_{0.25}$ (−0.72 mA cm^{-2}) > CoSe/GN$_{0.75}$ (−0.71 mA cm^{-2}) > CoSe (−0.68 mA cm^{-2}) > Pt (−0.52 mA cm^{-2}) > CoSe/GN$_{1.00}$ (−0.47 mA cm^{-2}). The higher cathodic current density of CoSe/GN nanohybrids is due to the higher active areas provided by graphene. The cathodic peak of CoSe/GN$_{1.0}$ is not well defined compared to those of other CoSe/GN nanohybrids. This may be attributed to the strong stacking effect of excessive graphene in the nanohybrids that veils the electrocatalytic active sites of CoSe nanoparticles. Hence, beyond the optimum concentration of graphene, it has a passive effect on the catalytic activity towards tri-iodide reduction.[16]

Fig. 6b shows that the peak current densities are in a linear relationship with the square root of the scan root, indicating that the electrocatalytic behaviour is dependent on the diffusion coefficient (D_n, cm^2 s^{-1}). The D_n of I_3^- can be estimated from the cathodic peak current density of cyclic voltammograms using the Randles–Sevcik equation:[17]

$$J_{pc} = K \cdot n^{3/2} \cdot A \cdot C \cdot D_n^{1/2} \cdot \upsilon^{1/2} \quad (3)$$

where J_{pc} represents the peak current density of Red$_2$ (mA cm^{-2}), K is the constant of 2.69×10^5, n is the number of electrons transferred in the redox event, A is the electrode area (cm^2), C represents the bulk concentration of I_3^- species (mol L^{-1}), and υ is the scan rate (V s^{-1}). The D_n values of I_3^- for platinum, CoSe and CoSe/GN nanohybrids are given in Table 1. The D_n shows the trend of CoSe/GN$_{0.50}$ (4.19×10^{-6} cm^2 S^{-1}) > CoSe/GN$_{0.25}$ (2.87×10^{-6} cm^2 S^{-1}) > CoSe/GN$_{0.75}$ (2.79×10^{-6} cm^2 S^{-1}) > CoSe (2.56×10^{-6} cm^2 S^{-1}) > Pt (1.49×10^{-6} cm^2 S^{-1}) > CoSe/GN$_{1.00}$ (1.22×10^{-6} cm^2 S^{-1}). The larger D_n of CoSe/GN$_{0.50}$ (4.19×10^{-6} cm^2 S^{-1}) arises due to the higher active surface area of CoSe/GN$_{0.50}$.[17] The CoSe nanoparticles anchored on the graphene sheets act as a spacer that prevents the restacking of graphene sheets thereby providing a higher active surface area and an efficient diffusion pathway for the electrolyte. At the mass ratio of CoSe : graphene = 1 : 0.25, the CoSe nanoparticles aggregate and there is no connection with graphene (Fig. 1c) which constrains the available active surface area. Beyond the mass ratio of 1 : 50, the enwrapment of the CoSe nanoparticles

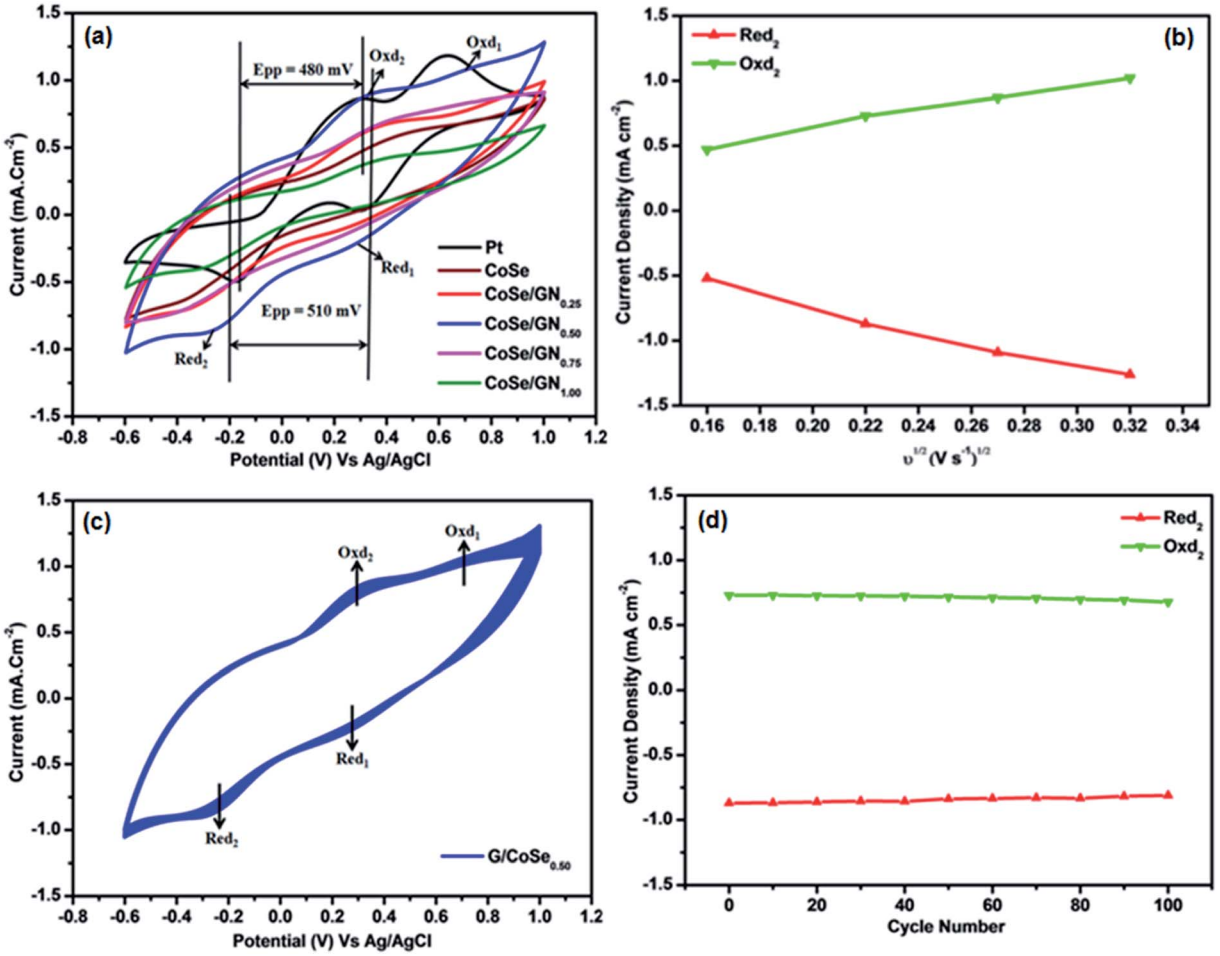

Fig. 6 (a) Cyclic voltammograms of platinum, CoSe and CoSe/GN nanohybrids at a scan rate of 50 mV s^{-1}; (b) the oxidation and reduction current densities of the $CoSe/GN_{0.50}$ nanohybrid electrode *vs.* the square root of scan rates; (c) cyclic voltammogram of $CoSe/GN_{0.50}$ nanohybrids up to 100 cycles at a scan rate of 50 mV s^{-1}; and (d) the relationship between the number of cycles and the maximum reduction peak current density for $CoSe/GN_{0.50}$ nanohybrids.

occurs due to the restacking of graphene which reduces the availability of active sites.

The separation (E_{pp}) between Oxd_2 and Red_2 peaks is inversely correlated with the electron transfer rate (K_s). A smaller E_{pp} indicates a higher K_s. The E_{pp} of $CoSe/GN_{0.50}$ (510 mV) is closer to that of platinum (480 mV), implying that the $CoSe/GN_{0.50}$ has faster redox kinetics and better electrocatalytic activity due to the homogeneously dispersed CoSe nanoparticles on the graphene surface, high surface area of graphene for CoSe anchoring, and high electrical conductivity of graphene. In addition, the $CoSe/GN_{0.50}$ nanocomposites exhibit high stability after 100 CV cycles, Fig. 6c and d. This indicates that the $CoSe/GN_{0.50}$ counter electrode is a remarkably good electrochemical catalyst for the reduction of I_3^-, having advantages of excellent electrochemical stability and strong adhesiveness on the FTO glass substrates.

The Tafel polarization studies were performed to test further the electrocatalytic capability of the CEs. Fig. 7 shows that the $CoSe/GN_{0.50}$ CE has a relatively larger slope for the anodic or cathodic polarization zone in comparison to other samples owing to its increased exchange current density (J_0) at the interface. The highest J_0 of the $CoSe/GN_{0.50}$ corresponds to the lower R_{ct} and highest catalytic activity, which is consistent with the electrochemical impedance (Fig. 5) and CV results (Fig. 6).

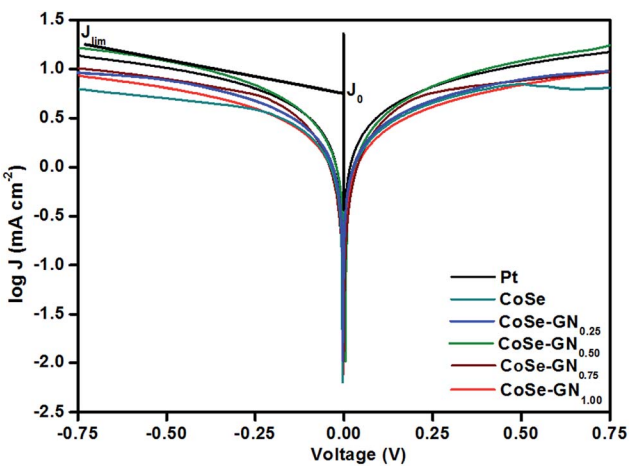

Fig. 7 Tafel polarization curves of symmetrical cells fabricated with platinum, CoSe and CoSe/GN nanohybrids.

Meanwhile, the J_0 can also be evaluated from the R_{ct} of the Nyquist plot according to eqn (4)[46] and the values are given in Table 1:

$$J_0 = \frac{RT}{nFR_{ct}} \quad (4)$$

where R is the gas constant, T is the absolute temperature, F is the Faraday constant and n is the number of electrons involved in the reduction of I_3^- to I^-, and R_{ct} is the charge transfer resistance. Additionally, the limiting current density (J_{lim}) can be obtained from the current density in the low slope and high potential region. The J_{lim} directly depends on the diffusion coefficient (D_n) according to eqn (5):[47]

$$D_n = \frac{lJ_{lim}}{2nFC} \quad (5)$$

where l is the spacer thickness, and C is the concentration of I_3^-. It is observed that the J_{lim} values of CoSe/GN nanohybrids and platinum are higher than that of the CoSe nanoparticles, suggesting that the CoSe/GN nanohybrids have a higher diffusion coefficient.[32] The higher diffusion coefficient is attributed to the presence of CoSe nanoparticles on the graphene nanosheets. The $CoSe/GN_{0.50}$ is found to have the highest J_{lim} due to the homogenous immobilization of highly dense CoSe nanoparticles on the graphene nanosheets, thereby reducing the diffusion resistance. The agglomeration of CoSe nanoparticles at the lower graphene concentration, and the π–π stacking of graphene at higher graphene concentration impedes the diffusion of the electrolyte to the inner active sites of CoSe nanoparticles, resulting in the decreased J_{lim}. Thus, the $CoSe/GN_{0.50}$ with the lowest diffusion resistance contributes most efficiently to the reduction of triiodide ions. Thus, the results from the electrochemical impedance, CV and Tafel measurements imply that the $CoSe/GN_{0.50}$ nanohybrids could serve as a less expensive alternative to platinum as CEs in DSSCs, Table 1.

Fig. 8 shows the Nyquist plots for DSSCs fabricated using platinum, CoSe and $CoSe/GN_{0.50}$ nanohybrids as counter electrodes. The inset shows the equivalent circuit used to analyze the Nyquist plots using EC lab software and their corresponding values are given in Table 2. In the equivalent circuit, R_s is the series resistance representing the resistance of the substrate, TiO_2 film, *etc.* The smaller arc in the high frequency region corresponds to the charge transfer resistance (R_{ct1}) and double layer capacitance (C_{dl1}) at the CE/electrolyte interface, while the larger semicircle at the intermediate frequency corresponds to the charge transfer resistance (R_{ct2}) and double layer capacitance (C_{dl2}) at the dye adsorbed TiO_2/electrolyte interface. The value of R_{ct1} for the $CoSe/GN_{0.50}$ nanohybrid CE is lower than that of the platinum counter electrode. This is due to the enhanced charge collection efficiency and higher triiodide reduction rate of $CoSe/GN_{0.50}$ nanohybrids. There is no significant change observed for the R_{ct2} values because both the DSSCs have the same photoanodes.

Table 2 EIS parameters of DSSCs fabricated with platinum, CoSe and $CoSe/GN_{0.50}$ nanohybrid CEs

CE	R_s (Ω)	R_{ct1} (F)	C_{dl1} (F)	R_{ct2} (Ω)	C_{dl2} (F)
Pt	5.36	2.96	0.17×10^{-6}	20.1	4.3×10^{-6}
CoSe	5.62	3.18	0.22×10^{-6}	20.1	3.6×10^{-6}
$CoSe/GN_{0.50}$	4.61	1.61	0.37×10^{-6}	19.6	5.5×10^{-6}

Fig. 9 shows the photocurrent density–voltage (J–V) curves of the DSSCs based on platinum, CoSe, and $CoSe/GN_{0.50}$ CEs obtained at a light intensity of 100 mW cm^{-2} under the standard global AM 1.5 irradiation. Their corresponding parameters are given in Table 3. The photovoltaic performance of the $CoSe/GN_{0.50}$ CE is superior to that of platinum and pure CoSe. The DSSCs fabricated with $CoSe/GN_{0.50}$ nanohybrids as CEs have a higher efficiency (9.27%) than those fabricated with platinum (7.68%) and CoSe (7.39%) CEs. The enhancement in the FF for DSSCs with $CoSe/GN_{0.50}$ is attributed to the decrease in the R_s and R_{ct}. Furthermore, the significant improvement of J_{sc} in the $CoSe/GN_{0.50}$ based CE is due to the highly conductive graphene that serves as a conductive pathway for electron transport. The graphene provides a shortcut for the electrons arriving from the external circuit to the CoSe and thereby increases the total current of the I^-/I_3^- redox reaction.

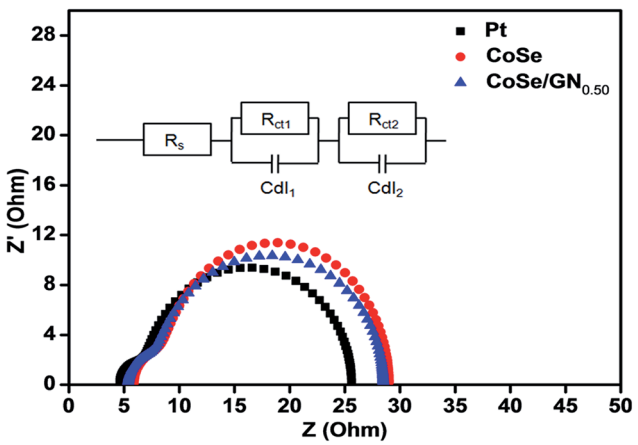

Fig. 8 Nyquist plots of DSSCs fabricated with platinum, CoSe and $CoSe/GN_{0.50}$ nanohybrid CEs.

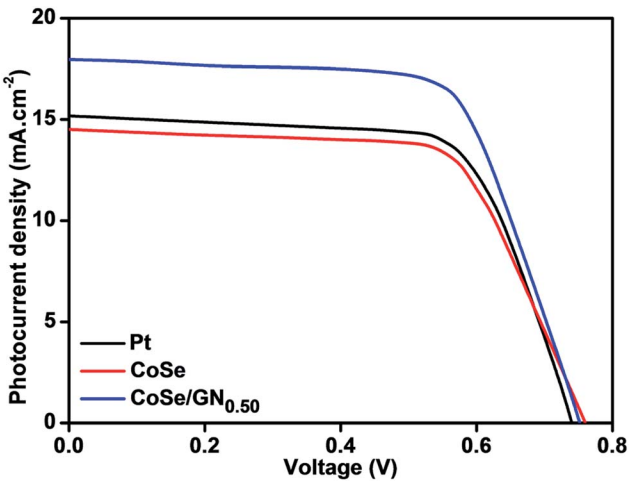

Fig. 9 Photocurrent density–voltage (J–V) curves of DSSCs fabricated with the platinum, CoSe and $CoSe/GN_{0.50}$ nanohybrid CEs.

Table 3 Photovoltaic parameters of DSSCs fabricated with platinum, CoSe and CoSe/$GN_{0.50}$ nanohybrid CEs

Counter electrodes	V_{oc} (V)	J_{sc} (mA cm^{-2})	FF	η (%)
Pt (standard)	0.74	15.18	0.684	7.68
CoSe	0.76	14.51	0.670	7.39
CoSe/$GN_{0.50}$	0.75	17.96	0.688	9.27

Fig. 10 illustrates the charge transfer mechanism of DSSCs fabricated with CoSe/$GN_{0.50}$ as the CE. The graphene functioned as the primary framework structure bridging all the secondary structure of CoSe nanoparticles together. The high surface area of graphene promotes a high number of CoSe nanoparticles to anchor on the surface of graphene and also increases the accessible contact area of the CoSe/GN CE with the electrolyte than that of CoSe. This leads to the reduction in the electron–hole recombination and thus enhances the efficiency of DSSCs.[15]

The CoSe/$GN_{0.50}$ is observed to exhibit 20% improvement in the photo-conversion efficiency than the standard Pt, Table 4, which is much higher than those of other reported binary metal selenides.[8–11,43] The significant improvement of PCE for CoSe/$GN_{0.50}$ compared to other reported bare metal selenides is due to the inclusion of graphene which acts as a linker to increase the electrical connection between the bare CoSe nanoparticles and thus enhances the overall performance of DSSCs. These significant improvements spotlight the prominent synergistic effect of the high electrocatalytic activity of CoSe and high electrical conductivity of graphene in the CoSe/GN nanohybrids.

4. Conclusion

CoSe/graphene nanohybrids were prepared successfully by an *in situ* hydrothermal reaction method and used as efficient counter electrodes for DSSCs. The stoichiometric ratio of CoSe was found to be $Co_{0.90}Se$. At the optimized mass ratio of CoSe/$GN_{0.50}$, the CoSe nanoparticles were homogeneously immobilized onto the graphene sheets. The enhanced electrochemical properties were due to the synergistic effects of CoSe and graphene. The CoSe/$GN_{0.50}$ nanohybrids reduced the charge transfer resistance which retarded the interfacial recombination, thereby enhancing the overall PCE of the DSSCs. The PCE of DSSCs with CoSe/$GN_{0.50}$ as the CE exhibited 20% improvement in the photo-conversion efficiency with respect to the

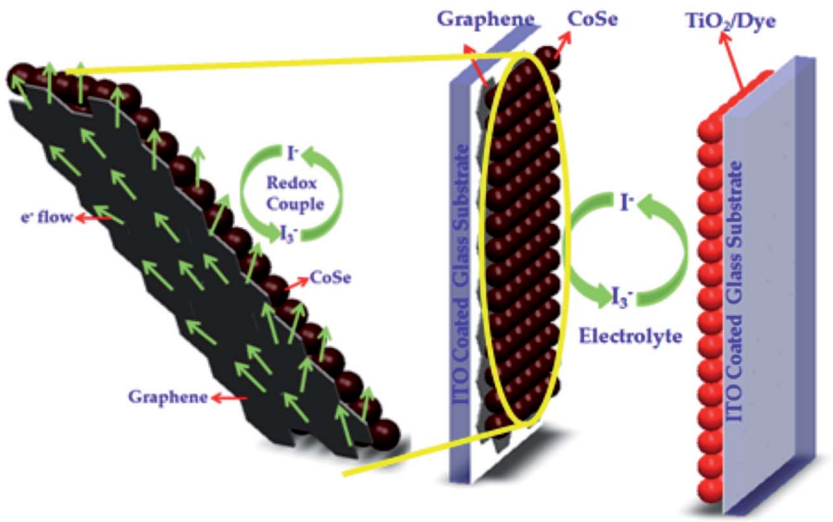

Fig. 10 Schematic representation of DSSC fabricated with CoSe/$GN_{0.50}$ as the CE and charge transfer mechanism in the CoSe/$GN_{0.50}$ based CEs.

Table 4 Comparison of photovoltaic performances of DSSCs based on CoSe/$GN_{0.50}$ obtained with the photovoltaic performances of DSSCs based on reported metal selenides

				Cell efficiency, η (%)			
Counter electrodes	V_{oc} (V)	J_{sc} (mA cm^{-2})	FF	Std. Pt	Prepared CE	% improvement in PCE	Ref.
$Co_{0.85}Se$	0.738	16.98	0.75	8.64	9.40	8	8
$Ni_{0.85}Se$	0.780	16.39	0.695	8.13	8.88	9	9
$Ni_{0.85}Se$	0.741	16.59	63.9	6.97	7.85	12	10
Ni_3Se_4@MeOH	0.746	16.27	0.69	8.03	8.31	3	11
$Co_{0.85}Se$	0.742	16.80	0.67	—	8.30	—	43
CoSe/$GN_{0.50}$	0.75	17.96	0.688	7.68	9.27	22	This work

standard Pt CE, which was much higher than those of other reported binary metal selenides.

Acknowledgements

The authors gratefully acknowledge the Council of Scientific and Industrial Research (CSIR), New Delhi (Ref. No. 01/2810/14/EMR-II, dt. 24/11/2014) for the financial support. Mr MV grateful to the Department of Science and Technology (DST), New Delhi for providing a fellowship under DST-Inspire Award (IF160290). Z. Guo appreciates the financial support from the University of Tennessee.

References

1 B. O'Regan and M. Gratzel, *Nature*, 1991, **353**, 737–740.
2 T. Liu, J. Hou, B. Wang, F. Bai, H. Chen, L. Gao, Y. Cao, H. He, J. Wang, N. Wang, G. Cao and Z. Guo, *J. Mater. Chem. A*, 2016, **4**, 10794–10800.
3 (*a*) M. Grätzel, *J. Photochem. Photobiol., C*, 2003, **4**, 145–153; (*b*) T. Xu, P. Wei, X. Ren, H. Liu, L. Chen, W. Tian, S. Liu and Z. Guo, *Mater. Lett.*, 2017, **195**, 100–103.
4 H. He, C. Zhang, T. Liu, Y. Cao, N. Wang and Z. Guo, *J. Mater. Chem. A*, 2016, **4**, 9362–9369.
5 E. Olsen, G. Hagen and S. Lindquist, *Sol. Energy Mater. Sol. Cells*, 2000, **63**, 267–273.
6 W. Chartarrayawadee, S. E. Moulton, D. Li, C. O. Too and G. G. Wallace, *Electrochim. Acta*, 2012, **60**, 213–223.
7 Z. Zhang, W. Li, M. Yuen, T.-W. Ng, Y. Tang, C.-S. Lee, X. Chen and W. Zhang, *Nano Energy*, 2015, **18**, 196–204.
8 (*a*) C. Alippi, *CAAI Transactions on Intelligence Technology*, 2016, **1**, 1–3; (*b*) H. Jin, Q. Chen, Z. Chen, Y. Hu and J. Zhang, *CAAI Transactions on Intelligence Technology*, 2016, **1**, 104–113; (*c*) F. Gong, H. Wang, X. Xu, G. Zhou and Z.-S. Wang, *J. Am. Chem. Soc.*, 2012, **134**, 10953–10958.
9 (*a*) J. Jia, J. Wu, Y. Tu, J. Huo, M. Zheng and J. Lin, *J. Alloys Compd.*, 2015, **640**, 29–33; (*b*) X. Zhang, H. Gao, M. Guo, G. Li, Y. Liu and D. Li, *CAAI Transactions on Intelligence Technology*, 2016, **1**, 4–13; (*c*) Z. Sun, L. Zhang, F. Dang, Y. Liu, Z. Fei, Q. Shao, H. Lin, J. Guo, L. Xiang, N. Yerra and Z. Guo, *CrystEngComm*, 2017, **19**, 3288–3298.
10 (*a*) Y. Duan, Q. Tang, B. He, R. Li and L. Yu, *Nanoscale*, 2014, **6**, 12601–12608; (*b*) M. Wang, K. Zhang, X. Dai, Y. Li, J. Guo, H. Liu, G. Li, Y. Tan, J. Zeng and Z. Guo, *Nanoscale*, 2017, DOI: 10.1039/C7NR02322G, in press; (*c*) J. Guo, H. Song, H. Liu, C. Luo, Y. Ren, T. Ding, M. A. Khan, D. P. Young, X. Liu, X. Zhang, J. Kong and Z. Guo, *J. Mater. Chem. C*, 2017, **5**, 5334; (*d*) H. Liu, M. Dong, W. Huang, J. Gao, K. Dai, J. Guo, G. Zheng, C. Liu, C. Shen and Z. Guo, *J. Mater. Chem. C*, 2017, **5**, 73–83; (*e*) H. Liu, J. Gao, W. Huang, K. Dai, G. Zheng, C. Liu, C. Shen, X. Yan, J. Guo and Z. Guo, *Nanoscale*, 2016, **8**, 12977–12989; (*f*) H. Liu, W. Huang, J. Gao, K. Dai, G. Zheng, C. Liu, C. Shen, X. Yan, J. Guo and Z. Guo, *Appl. Phys. Lett.*, 2016, **108**, 011904.
11 (*a*) C.-T. Lee, J.-D. Peng, C.-T. Li, Y.-L. Tsai, R. Vittal and K.-C. Ho, *Nano Energy*, 2014, **10**, 201–211; (*b*) Y. Guo, T. Liu, N. Wanga, Q. Luo, H. Lin, J. Li, Q. Jiang, L. Wu and Z. Guo, *Nano Energy*, 2017, **38**, 193; (*c*) T. Liu, L. Yu, H. Liu, Q. Hou, C. Wang, H. He, J. Li, N. Wang, J. Wang and Z. Guo, *J. Mater. Chem. A*, 2017, **5**, 4292–4299; (*d*) S. Padhy and S. Panda, *CAAI Transactions on Intelligence Technology*, 2017, **2**, 12–25.
12 H. Bi, W. Zhao, S. Sun, H. Cui, T. Lin, F. Huang, X. Xie and M. Jiang, *Carbon*, 2013, **61**, 116–123.
13 X. Duan, Z. Gao, J. Chang, D. Wu, P. Ma, J. He, F. Xu, S. Gao and K. Jiang, *Electrochim. Acta*, 2013, **114**, 173–179.
14 (*a*) T. Xu, L. Chen, Z. Guo and T. Ma, *Phys. Chem. Chem. Phys.*, 2016, **18**, 27026–27050; (*b*) L. Zhang, Q. Zhang, H. Xie, J. Guo, H. Lyu, Y. Li, Z. Sun, H. Wang and Z. Guo, *Appl. Catal., B*, 2017, **201**, 470–478.
15 S. Das, P. Sudhagar, S. Nagarajan, E. Ito, S. Lee, Y. Kang and W. Choi, *Carbon*, 2012, **50**, 4815–4821.
16 J. Shen, R. Cheng, Y. Luo, Y. Chen, X. Chen, Z. Sun and S. Huang, *J. Solid State Electrochem.*, 2015, **19**, 1045–1052.
17 C.-J. Liu, S.-Y. Tai, S.-W. Chou, Y.-C. Yu, K.-D. Chang, S. Wang, F. Chien, J.-Y. Lin and T.-W. Lin, *J. Mater. Chem.*, 2012, **22**, 21057–21064.
18 S. Hébert, W. Kobayashi, H. Muguerra, Y. Bréard, N. Raghavendra, F. Gascoin, E. Guilmeau and A. Maignan, *Phys. Status Solidi A*, 2013, **210**, 69–81.
19 S. Flamee, R. Dierick, M. Cirillo, D. Genechten, T. Aubert and Z. Hens, *Dalton Trans.*, 2013, **42**, 12654–12661.
20 S. Tyrrell, G. Behrendt, Y. Liu and P. Nockemann, *RSC Adv.*, 2014, **4**, 36110–36116.
21 H. Liu, J. Zhang, X. Zheng, G. Liu, H. Hu, W. Pan, C. Liu, Q. Hao and H. Chen, *CrystEngComm*, 2016, **18**, 6860–6866.
22 I. S. Lyubutin, C.-R. Lin, K. O. Funtov, T. V. Dmitrieva, S. S. Starchikov, Y.-J. Siao and M.-L. Chen, *J. Chem. Phys.*, 2014, **141**, 44704.
23 Y. Xu, H. Bai, G. Lu, C. Li and G. Shi, *J. Am. Chem. Soc.*, 2008, **130**, 5856–5857.
24 W. S. Hummers and R. E. Offeman, *J. Am. Chem. Soc.*, 1958, **80**, 1339.
25 H. Bisht, H. T. Eun, A. Mehrtens and M. A. Aegerter, *Thin Solid Films*, 1999, **351**, 109–114.
26 K. Saranya, N. Sivasankar and A. Subramania, *RSC Adv.*, 2014, **4**, 36226–36233.
27 E. Vijayakumar, A. Subramania, Z. Fei and P. J. Dyson, *J. Appl. Polym. Sci.*, 2015, **132**, 42032.
28 K. Saranya, A. Subramania and N. Sivasankar, *RSC Adv.*, 2015, **5**, 43611–43619.
29 B. Yang, X. Zuo, P. Chen, L. Zhou, X. Yang, H. Zhang, G. Li, M. Wu, Y. Ma, S. Jin and X. Chen, *ACS Appl. Mater. Interfaces*, 2015, **7**, 137–143.
30 V. Elayappan, V. Murugadoss, S. Angaiah, Z. Fei and P. Dyson, *J. Appl. Polym. Sci.*, 2015, **132**, 42777.
31 Z. Salam, E. Vijayakumar, A. Subramania, N. Sivasankar and S. Mallick, *Sol. Energy Mater. Sol. Cells*, 2015, **143**, 250–259.
32 H. Chen, T. Liu, J. Ren, H. He, Y. Cao, N. Wang and Z. Guo, *J. Mater. Chem. A*, 2016, **4**, 3238–3244.
33 A. Subramania, E. Vijayakumar, N. Sivasankar, S. A. R. Priya and K.-J. Kim, *Ionics*, 2013, **19**, 1649–1653.

34 G. Wang, J. Zhang, S. Kuang, S. Liu and S. Zhuo, *J. Power Sources*, 2014, **269**, 473–478.
35 L.-f. Zhang and C.-y. Zhang, *Nanoscale*, 2013, **6**, 1782–1789.
36 C. Mattevi, G. Eda, S. Agnoli, S. Miller, A. K. Mkhoyan, O. Celik, D. Mastrogiovanni, G. Granozzi, E. Garfunkel and M. Chhowalla, *Adv. Funct. Mater.*, 2009, **19**, 2577–2583.
37 H. Chen, S. Chen, M. Fan, C. Li, D. Chen, G. Tian and K. Shu, *J. Mater. Chem. A*, 2015, **3**, 23653–23659.
38 C. E. M. Campos, J. C. de Lima, T. A. Grandi, K. D. Machado and P. S. Pizani, *Phys. B*, 2002, **324**, 409–418.
39 C. E. M. Campos, J. C. de Lima, T. A. Grandi, K. D. Machado, V. Drago and P. S. Pizani, *Solid State Commun.*, 2004, **131**, 265–270.
40 J. Shen, Y. Hu, M. Shi, N. Li, H. Ma and M. Ye, *J. Phys. Chem. C*, 2010, **114**, 1498–1503.
41 M. Zhu, X. Li, W. Liu and Y. Cui, *J. Power Sources*, 2014, **262**, 349–355.
42 M. M. Lucchese, F. Stavale, E. H. Ferreira, C. Vilani, M. V. O. Moutinho, R. B. Capaz, C. A. Achete and A. Jorio, *Carbon*, 2010, **48**, 1592–1597.
43 Y. Duan, Q. Tang, B. He, Z. Zhao, L. Zhu and L. Yu, *J. Power Sources*, 2015, **284**, 349–354.
44 J.-F. Zhao, J.-M. Song, C.-C. Liu, B.-H. Liu, H.-L. Niu, C.-J. Mao, S.-Y. Zhang, Y.-H. Shen and Z.-P. Zhang, *CrystEngComm*, 2011, **13**, 5681–5684.
45 L. Sun, Y. Bai, N. Zhang and K. Sun, *Chem. Commun.*, 2014, **51**, 1846–1849.
46 Z. Li, F. Gong, G. Zhou and Z.-S. Wang, *J. Phys. Chem. C*, 2013, **117**, 6561–6566.
47 S.-Y. Tai, C.-F. Chang, W.-C. Liu, J.-H. Liao and J.-Y. Lin, *Electrochim. Acta*, 2013, **107**, 66–70.